Remote Sensing Image Recovery and Enhancement by Joint Blind Denoising and Dehazing

Yan Cao, Jianchong Wei, Sifan Chen, Baihe Chen, Zhensheng Wang, Zhaohui Liu, and Chengbin Chen

***Abstract*—Due to the hazy weather and the long-distance imaging path, the captured remote sensing image (RSI) may suffer from detail loss and noise pollution. However, simply applying dehazing operation on a noisy hazy image may result in noise amplification. Therefore, in this article, we propose joint blind denoising and dehazing for RSI recovery and enhancement to address this problem. First, we propose an efficient and effective noise level estimation method based on quad-tree subdivision and integrate it into fast and flexible denoising convolutional neural network for blind denoising. Second, a multiscale guided filter decomposes the denoised hazy image into base and detailed layers, separating the initial details. Then, the dehazing procedure using the corrected boundary constraint is implemented in the base layer, while a nonlinear sigmoid mapping function enhances the detailed layers. The last step is to fuse the enhanced detailed layers and the dehazed base layer to get the final result. Using both synthetic remote sensing hazy image (RSHI) datasets and real-world RSHI, we perform comprehensive experiments to evaluate the proposed method. Results show that our method is superior to well-known methods in both dehazing and joint denoising and dehazing tasks.**

***Index Terms*—Image dehazing, image denoising, remote sensing.**

I. Introduction

REMOTE sensing imagery has been extensively used in various applications, such as geoscience, military, agriculture, and the environment. However, the remote sensing image (RSI) has much more complex atmospheric conditions like haze, water vapor, cloud, and noise, than the ground imagery due to the long imaging path and the wide field-of-view. Thus, the captured RSIs are usually suffered from serious degradation like detail loss, blurring, and color distortion, which severely constrained the performance of remote sensing vision applications. Hence, much attention has been paid to developing reliable and efficient RSI recovery algorithms, such as dehazing, denoising, and super-resolution [1], [2], [3], [4], [5], [6], [7].

For remote sensing image dehazing (RSID) task, the image degradation under hazy conditions can be formulated by the atmospheric scattering model (ASM) [8]. Therefore, there are two main categories for the existing dehazing algorithms: model-based methods and nonmodel-based methods. The model-based dehazing methods recover the clear image based on the ASM, while the nonmodel-based methods directly infer the haze-free image without considering the degradation principle. Traditionally, the nonmodel-based methods apply image enhancement operations to improve the image's quality in the spatial or frequency domain [2], [5]. For example, Dharejo et al. [9] enhanced the remote sensing hazy image (RSHI) using a piecewise linear transformation and corrected the color distortion with histogram equalization. Although the image enhancement operations can improve the hazy image's visual quality, the recovered image may result in overenhancement and color distortion, especially in real-world RSHI. Furthermore, they cannot achieve real dehazing without considering the hazy image's degradation process. In recent years, the convolutional neural network (CNN) has been widely used in RSID task [10], [11], taking it as learning-based dehazing method. Without considering the haze imaging degradation principle, some learning-based dehazing methods take the RSID as an image-to-image translation task using a generative adversarial network (GAN). For example, Zheng et al. [12] proposed an enhanced attention-guided GAN, which can be trained without paired RSHI. Chen et al. [13] presented a memory-oriented GAN for RSID to handle real-world nonuniform haze conditions. Although the GAN-based dehazing methods benefit from preventing the labor-intensive paired data collection, they cannot well restore the image's full details and the unsupervised learning process is hard to converge.

For model-based dehazing methods, the ASM [8] is widely adopted for the haze removal task, which can be expressed as follows:

$$I(x) = J(x)t(x) + A(1 - t(x)) \tag{1}$$

where I is the captured hazy image by satellites, J is the recovered clear image, and A and t represent the global atmospheric light and the transmission map, respectively. In order to recover J from I, the t and A should be estimated. However, given only a hazy image I is insufficient to recover the clear image. Thus, some hazy image priors are proposed to solve the problem.

Manuscript received 29 January 2023; revised 19 February 2023; accepted 8 March 2023. Date of publication 13 March 2023; date of current version 29 March 2023. This work was supported by the Education and Scientific Research Project for Middle-Aged and Young Teachers in Fujian Province under Grant JAT200370. *(Corresponding author: Chengbin Chen.)*

Yan Cao is with the College of Finance, Fujian Jiangxia University, Fuzhou 350108, China, and also with the College of Forestry, Fujian Agriculture and Forestry University, Fuzhou 350002, China (e-mail: caoyan_0809@fjjxu.edu.cn).

Jianchong Wei is with the College of Electronics and Information Science, Fujian Jiangxia University, Fuzhou 350108, China (e-mail: jjasonway@fjjxu.edu.cn).

Sifan Chen is with the College of Physics and Information Engineering, Fuzhou University, Fuzhou 350025, China (e-mail: 201127011@fzu.edu.cn).

Baihe Chen is with the College of Modern Information Industry, Guangzhou College of Commerce, Guangzhou 511363, China (e-mail: chenpingchang0508@gmail.com).

Zhensheng Wang, Zhaohui Liu, and Chengbin Chen are with the Department of Mathematics and Theories, Peng Cheng Laboratory, Shenzhen 518066, China (e-mail: wangzhsh@pcl.ac.cn; liuchh@pcl.ac.cn; ccb_net@qq.com).

Digital Object Identifier 10.1109/JSTARS.2023.3255837

For example, He et al. [14] observed the dark channel prior (DCP) from the statistics of a large amount of haze-free image. The DCP is simple and effective for dehazing, but it may fail in areas like sky regions or large white objects. Recently, CNN has been applied to solve the ASM. Zhang et al. [15] designed a densely connected pyramid dehazing network to jointly infer the parameters in the ASM.

Once the t and A are obtained, the clear image can be recovered by reversing the (1). However, most of the existing model-based methods neglect the noise term when conducting the image dehazing, but noise is inevitable during image sensing, especially in poor environmental conditions, like haze. Therefore, by taking the additive noise into account, (1) can be reformulated as follows:

$$I(x) = J(x)t(x) + A(1 - t(x)) + n \tag{2}$$

where n is generally additive white Gaussian noise (AWGN) [16]. To recover a haze-free image as per the degradation principle, t and A should be estimated by a well-designed dehazing method. Then, the final recovered haze-free image J can be calculated as follows:

$$\hat{J}(x) = \frac{I(x) - A}{t(x)} + A + \frac{n}{t(x)} = J(x) + \frac{n}{t(x)}. \tag{3}$$

Note that t is a positive decimal less than 1, so the last term in (3) amplifies the noise (n). Therefore, model-based dehazing methods can effectively remove haze, but noise amplification may introduce undesirable results.

To this end, this article aims to overcome the detail lost and noise amplification issues for RSI recovery by joint blind denoising and dehazing. First, we propose an efficient and effective noise level estimation method based on quad-tree subdivision that can be integrated into fast and flexible denoising convolutional neural network (FFDNet) [17] to achieve blind denoising. So the image denoising is performed before the following dehazing procedure. Then, the denoised hazy image is decomposed into a base layer and detailed layers by a multiscale guided filter (GF). To prevent detailed information loss, dehazing using a corrected boundary constraint is only implemented in the base layer, while a sigmoid-based nonlinear mapping function enhances the detailed layers. Finally, the enhanced detail layers and dehazed base layer are fused to produce the haze-free image. In summary, our main contributions are as follows:

1) To tackle the problem of noise amplification of dehazing, we propose an efficient and effective noise level estimation method based on a quad-tree subdivision algorithm. And we integrate it into FFD-Net to achieve blind denoising as the preprocessing before the following dehazing.
2) To preserve image details, we decompose the hazy image into a base layer and detailed layers using a multiscale GF, so the dehazing and detail enhancement are conducted separately. We improve the boundary constraint dehazing by introducing a tolerance factor to solve the overenhancement of the sky region. And an adaptive sigmoid-based nonlinear function is proposed for detailed layers enhancement.
3) Comprehensive experiments were conducted to show that the proposed method has superior performance in RSI denoising, dehazing, and joint denoising and dehazing.

II. Related Work

A. Single Image Dehazing

The existing image dehazing methods can be categorized into two groups: one is classic dehazing methods, and the other is learning-based dehazing methods. For classic dehazing methods, some try to improve the visual quality of the hazy image through image enhancement. For example, Dharejo et al. [9] enhanced the RSHI using a piecewise linear transformation and corrected the color distortion with histogram equalization. Ju et al. [18] integrated the traditional gamma correction into the dehazing task to boost efficiency. In order to improve the image's overall contrast, Ni et al. [19] developed a linear intensity enhancement algorithm based on local property analysis. Rather than simply improving the visual quality of the hazy image, some methods propose various hazy image priors to tackle the ill-posed dehazing problem, such as the DCP [14], nonlocal prior [20], and color attenuation prior [21]. However, the hazy image prior may not be sufficient to handle the complex hazy situations. For instance, the DCP fails in processing hazy image with a bright sky and may introduce undesired artifacts.

In recent years, CNN has been dramatically applied to solve the RSID problem, termed as learning-based methods. Jiang et al. [22] integrated the wavelet transform (WT) into the CNN to remove the nonuniform haze in RSHI. Dong et al. [23] developed a two-branch network by combining the novel transformer and ResNet for RSHI. The dehazed results embrace the advantages of better detail preservation and color consistency. Similarly, Chen et al. [24] presented an end-to-end dehazing network based on hybrid high-resolution learning to recover the fine spatial details of RSHI. Although learning-based dehazing methods have met with some success in improving performance, the high computation cost of the training process limits their application. Furthermore, since many manual synthetic datasets are required for training, these methods are unsuitable for removing haze caused by complex remote sensing imaging degradations, and may fail in recovering real-world RSHI.

B. Single Image Denoising

Image denoising is one of the most fundamental preprocessing tasks in low-level computer vision [25]. Dabov et al. proposed block-matching 3-D filtering (BM3D) [26], which uses collaborative filtering to group similar 2-D blocks into 3-D data arrays. Given its strong denoising performance, BM3D has become the gold standard for single image denoising. Similar to BM3D, many other transform domain filters have been used for dehazing, including Fourier transform [27] and WT [28].

Owing to the large modeling capacity and advanced network design, many CNN-based methods have emerged for image denoising [29]. Zhang et al. [30] proposed a denoising convolutional neural network (DnCNN), which can handle blind

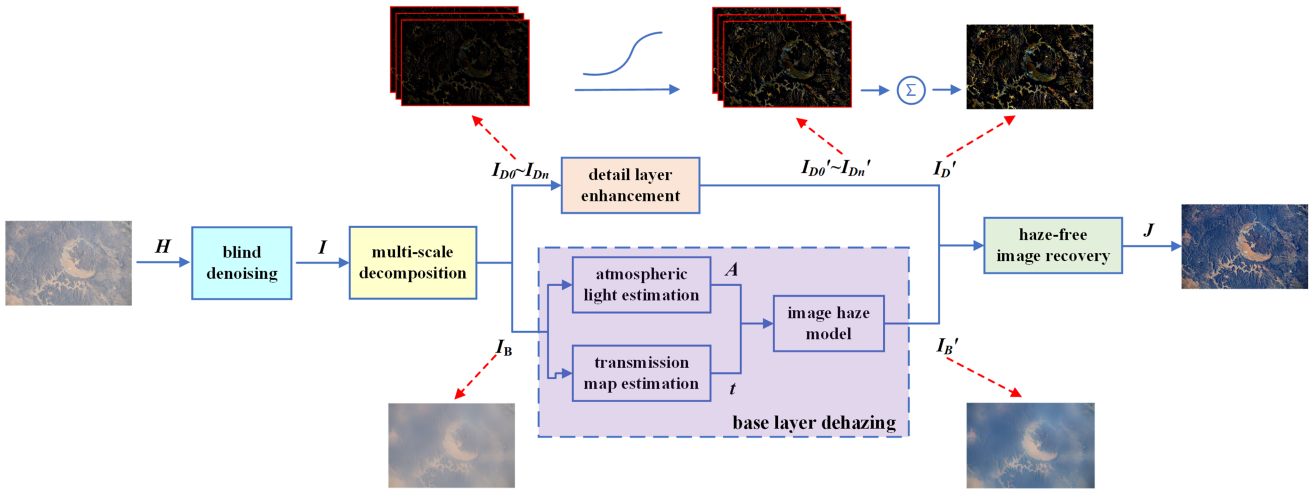

Fig. 1. Flowchart of the proposed dehazing method. H is the hazy input image. I is the denoised hazy image, which is decomposed into the base layer I_B and the detailed layers $I_{D0} - I_{Dn}$ by a multiscale decomposition module. I'_D and I'_B are the enhanced detailed layer and the dehazed base layer, respectively, and J is the final recovered haze-free image.

Gaussian denoising and achieve competitive performance. Feng et al. [31] implemented a restoration GAN with ResNet and DenseNet in the WT domain to restore high-quality RSI. In Zhang et al.'s work [17], a FFDNet was presented, which has better computational efficiency than BM3D. By incorporating the traditional denoising method into the network design, Ren et al. [32] proposed a novel end-to-end deep denoising network, named DeamNet. Although DeamNet can achieve superior performance to DnCNN and FFDNet, the lower computation efficiency constrains its application.

C. Joint Image Denoising and Dehazing

On hazy days, noise corruption is inevitable and the model-based dehazing process amplifies the noise. Therefore, much research [5], [16], [33], [34], [35], [36], [37] has proposed joint image denoising and dehazing methods. Based on the mechanism, such methods can be categorized into three groups: 1) cascade denoising and dehazing methods, 2) simultaneous denoising and dehazing methods, and 3) image-decomposition-based methods. Erik Matlin et al. [35] discussed the issue of the removal of haze and noise, and concluded that when the noise level is precisely known *a priori*, category 1 methods perform better than category 2 methods.

In category 1, Xu et al. [38] designed a slimmer and deeper network architecture for denoising and dehazing. Likewise, Su et al. [37] proposed a two-stage U-Net-based cascaded denoising and dehazing net to reduce haze and noise in a cascading pattern. However, both of their networks are bulky, and the training process is time-consuming. In category 2, Wu et al. [16] integrated noise reduction and haze-free image recovery by learning an interleaved cascade of shrinkage fields. However, this method cannot handle severely noisy and hazy images. In category 3, Liu et al. [34] separated the hazy image into high-frequency and low-frequency parts using multiscale wavelet decomposition. A similar approach was proposed by HSU's work [36], and although this approach removes haze in low-frequency areas, denoising alone in high-frequency parts is not sufficient. Liu et al. [5] proposed another decomposition strategy based on the total variation. The DCP and color block-matching 3-D filtering prior is selected for nighttime image dehazing and denoising, respectively.

III. Methodology

The flowchart of the proposed joint dehazing and dehazing method is shown in Fig. 1. A blind denoising module based on FFDNet [17] first preprocesses the hazy input image H to obtain the denoised image I. Then, in the multiscale decomposition module, I is decomposed into the base layer I_B and the multiscale detailed layers $I_{D0} - I_{Dn}$ using the multiscale GF. For detailed layers, an adaptive nonlinear mapping is performed for enhancement in each scale of the detailed layer to obtain I'_D. In the base layer dehazing module, atmospheric light A is estimated using a quad-tree subdivision algorithm. The transmission map t is recovered using the corrected boundary constraint and refined by the weighted GF. When A and t are obtained, the dehazed base layer I'_B can be obtained through ASM. Finally, I'_B and I'_D are fused to recover the haze-free image J.

A. Blind Denoising

Due to the influence of haze and image capture system, there is inevitably much noise in hazy images, and most of it is additive gaussian white noise (AGWN) [16]. Moreover, it can be inferred from (3) that the process of dehazing amplifies the noise signal level. Therefore, image denoising is necessary before dehazing. However, in many denoising methods [17], [26], [39] with a strong performance, the noise level is regarded as a known input, which confines their application to real-world noisy images with an unknown noise level. Furthermore, Zhang et al. [17] observed that the denoising performance of a nonblind denoising model can be improved with a known noise level map because additional information is provided as the input. Therefore, accurate noise level estimation for image denoising is

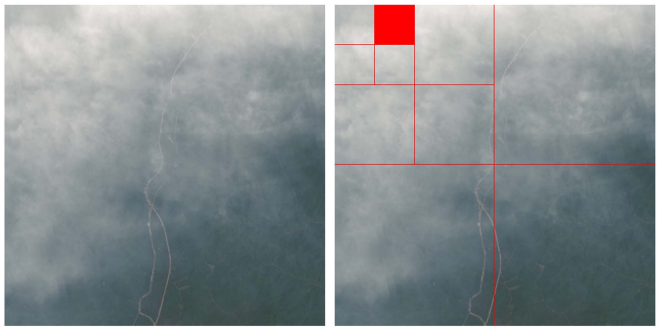

Fig. 2. Result of the quad-tree subdivision. (a) RSHI. (b) Quad-tree subdivision result.

important. However, though many AGWN noise level estimation methods [7], [40], [41] have been proposed, their efficiency and performance should be improved. To this end, we developed an efficient and effective noise level estimation method based on a quad-tree subdivision for hazy image denoising.

Inspired by the patch-based image denoising method [40], [41], the main issue of noise level estimation is correctly selecting flat and textureless patches in the image. According the HI's properties, the haziest patch is suitable for noise level estimation. Therefore, we determine the best patch by a quad-tree subdivision algorithm [3]. Given a hazy image, it is divided into four blocks and we calculate the score for each block by

$$S(p_i) = \text{mean}(p_i) - \text{std}(p_i) \tag{4}$$

where p_i is the ith block, and $i \in \{1, 2, 3, 4\}$. The block with the highest score will be further divided and we repeat this until the image block's size is under a threshold. The thicker the haze in the image, the larger the mean value of the corresponding block pixel, and the smoother the image block, the smaller the corresponding pixel variance. Thus, the block with the highest score is the haziest and most textureless. We empirically set the predefined threshold as 1/16 of the original image size to make the algorithm adapt to images with different resolutions. As shown in Fig. 2, the last selected block I_{final} marked in red is the flattest and most textureless, so it is used for further evaluation.

The following noise level estimation method is motivated by [7], which uses the eigenvalues of the covariance matrix within an image to estimate the true noise variance. Assuming the image size of I_{final} is $H \times W \times c$. We first decompose it into a number of patches $X_s = \{x_t\}_{t=1}^{s}$ with a patch size $d = 1$; that is, we regard each pixel as a patch. Thus, X_s contains $s = H \times W$ patches of the size $1 \times 1 \times c$. We select a patch size $d = 1$, which is different from that in Chen's method [7], for two reasons: 1) the selected image block (I_{final}) is flat and textureless, and 2) a small patch size reduces computational complexity. To simplify the calculation, X_s is reshaped as a vector with a size of $c \times s$. Then, we obtain the covariance matrix by

$$\sum_x = \frac{1}{s} \sum_{t=1}^{s} (x_t - \mu)(x_t - \mu)^T \tag{5}$$

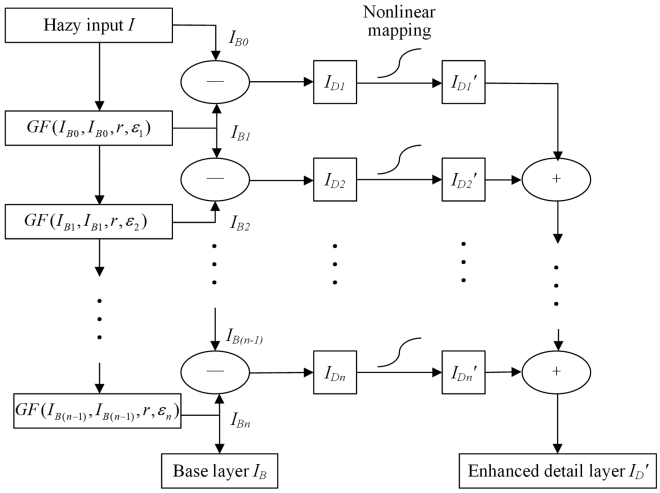

Fig. 3. Diagram of multiscale decomposition and detailed layer enhancement.

where $\mu = \frac{1}{s} \sum_{t=1}^{s} x_t$. Finally, the median value of the eigenvalues $\{\lambda_i\}_{i=1}^{c}$ of the covariance matrix is selected as the estimated noise level. Taking speed and performance into account, we integrate the proposed noise level estimation algorithm into FFDNet [17] for hazy image denoising.

B. Multiscale Decomposition and Detailed Layer Enhancement

The GF [42] is an edge-preserving smoothing image filter, which can be expressed as follows:

$$O = \text{GF}(I, G, r, \varepsilon) \tag{6}$$

where I and G are the input image and the guidance image, respectively. The regularization parameter ε is a smoothing factor that determines whether a patch with radius r in I should be preserved or smoothed based on the patch variance in G. Therefore, the GF selectively smooths the input image I based on the structure of the guidance image G.

When $I \equiv G$ in (6), the GF acts as an edge-preserving mean filter. Therefore, the details of image I can be extracted by iteratively filtering the hazy image with multiple smoothing scales $\varepsilon = \{\varepsilon_1, \varepsilon_2 \cdots, \varepsilon_n\}$, $(\varepsilon_1 < \varepsilon_2 \cdots < \varepsilon_n)$, which can be expressed as follows:

$$I_{Bi} = GF(I_{B(i-1)}, I_{B(i-1)}, r, \varepsilon_i) \quad i = 1, 2, \ldots, n \tag{7}$$

$$I_{Di} = I_{Bi} - I_{B(i-1)} \quad i = 1, 2, \ldots, n \tag{8}$$

where I_{Bi} is the filtered base layer with the associated smoothing scales ε_i, and the initial image I_{B0} is the hazy input image. The difference between the current base layer I_{Bi} and the previous base layer $I_{B(i-1)}$ is the filtered detailed layer I_{Di}. In addition, the last filtered image I_{Bn} is selected as the final base layer for further dehazing. An illustration of the multiscale decomposition is shown in Fig. 3.

A linear stretch on grayscale is simple but effective for enhancing the multiscale detailed layers. However, it has overenhanced details. Therefore, an adaptive nonlinear transform based on the sigmoid function is selected for detailed layer enhancement

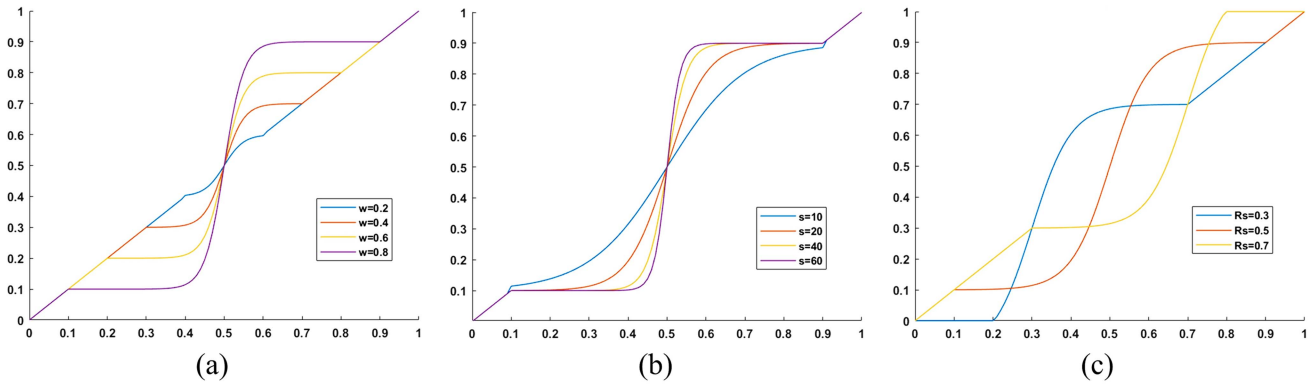

Fig. 4. Functional graphs of sigmoid-based nonlinear mapping with different parameters. (a) Change w from 0.2 to 0.8 ($R_s = 0.5, s = 40$). (b) Change s from 10 to 60 ($R_s = 0.5, w = 0.8$). (c) Change R_s from 0.3 to 0.7 ($s = 40, w = 0.8$).

without introducing much noise [43], which can be expressed as follows:

$$F(R) = \begin{cases} \frac{w}{1+e^{-s(R-R_s)}} + R_s - w, & R_s - 0.5w < R < R_s + 0.5w \\ R, & \text{otherwise} \end{cases} \tag{9}$$

where R is the image to be enhanced, i.e., the detailed layer I_{Di}. w indicates the width of the nonlinear region centered at R_s. Parameter s is the scale factor, which determines the enhancement level. The functional graphs with different parameters are illustrated in Fig. 4. As shown, a small change in the value of s has a significant impact on the shape of the graph. The larger the value of s, the stronger the enhancement. The width of the nonlinear region increases as w increases. R_s determines the center of the nonlinear region, which indicates that the pixels in the darker area are enhanced when it is small. Otherwise, it enhances the brighter areas. To achieve adaptive enhancement, we choose $s = 50(R_{\max} - R_{\min})$, $R_s = \text{mean}(R)$, $w = 0.8$, $R_{\max} = \max(R)$, and $R_{\min} = \min(R)$. Finally, the enhanced detailed layer I'_D is calculated by summing the enhanced output of each detailed layer, expressed as expressed follows:

$$I'_D = \sum_{i=1}^{n} F(I_{Di}). \tag{10}$$

C. Base Layer Dehazing and Haze-Free Image Reconstruction

In order to recover the clear image using (3), the A and t should be estimated. Typically, A is a constant in a hazy image and the value is close to the brightest pixel intensity. In literature, Tan et al. [44] naively selected the brightest pixel in the hazy image as the estimated atmospheric light. He et al. [14] picked the top 0.1% of the brightest pixels in the dark channel as the atmospheric light. However, these methods may have large errors when there are objects whose pixel intensity is higher than the atmospheric light. According to the noise level estimation, we estimate atmospheric light based on two characteristics: high intensity and no texture. Therefore, the mean value of the last highest score region I_{final} by quad-tree subdivision is selected to estimate A.

According to the boundary constraint proposed by Meng et al. [10], the scene radiance of a hazy image is always bounded [45]; that is

$$C_0 \le J(x) \le C_1 \tag{11}$$

where C_0 and C_1 are the lower and upper bounds of the given image, respectively. From (3), (11) can be rewritten as follows:

$$C_0 \le \frac{I(x) - A(1 - t(x))}{t(x)} \le C_1. \tag{12}$$

Thus, the solution of (12) for each color channel is given by the following inequalities:

$$t(x) \ge \frac{A^c - I^c(x)}{A^c - C_0^c} \quad \text{and} \quad t(x) \ge \frac{I^c(x) - A^c}{C_1^c - A^c} \tag{13}$$

where $c \in \{r, g, b\}$.

Therefore, the lower bound of $t(x)$ can be computed by

$$t_b(x) = \min \left\{ \max_{c \in \{r,g,b\}} \left(\frac{A^c - I^c(x)}{A^c - C_0^c}, \frac{A^c - I^c(x)}{A^c - C_1^c} \right), 1 \right\}. \tag{14}$$

Unlike He et al.'s method [14], Meng et al.'s [45] method proposes a new patchwise transmission, which is given as follows:

$$t(x) = \min_{y \in \omega_x} \max_{z \in \omega_y} t_b(z). \tag{15}$$

As shown in Fig. 5(b), the estimated transmission map $t(x)$ is coarse. Therefore, Meng et al. [45] proposed a weighted L1-norm-based contextual regularization method to refine the rough transmission map estimated by boundary constraint. However, the large computation complexity is the primary problem with this method, and overenhancement may occur in bright areas. For example, the sky region of the image dehazed by Meng's method [45] is overenhanced in Fig. 5(d). On this account, we use the weighted guided filter [46] for the transmission map refinement to boost efficiency. The refined transmission map is shown in Fig. 5(c), and the image dehazed using the refined transmission map is shown in Fig. 5(e). However, it still suffers from overestimated haze in bright areas [see the bright sky in Fig. 5(e)]. The boundary constraint fails in bright areas because there are no pixels whose values are close to C_0 or C_1. Therefore,

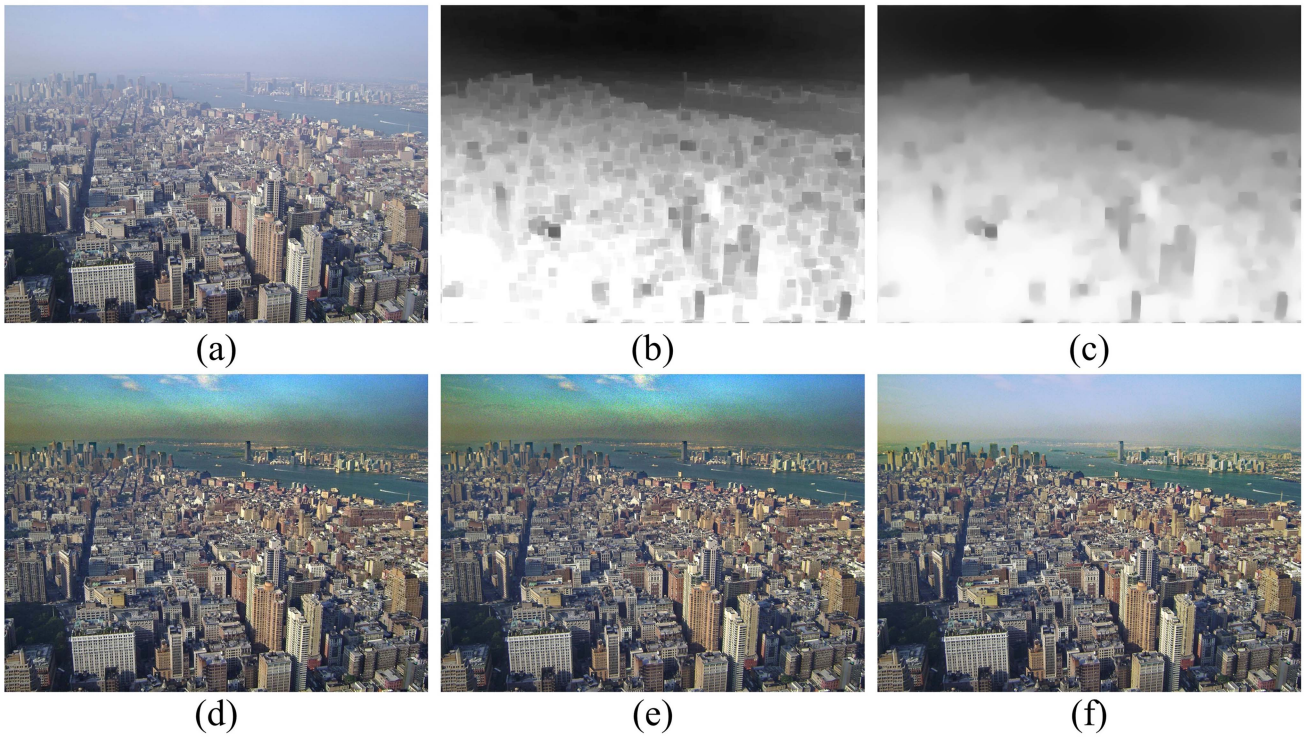

Fig. 5. Diagram of multiscale decomposition and detailed layer enhancement. Image dehazing using corrected boundary constraint ($C_0 = (20, 20, 20)^T$, $C_1 = (300, 300, 300)^T$, patch size: 15×15). (a) Input hazy image. (b) Patchwise transmission map $t(x)$ by boundary constraint. (c) Refined transmission map by the WGF. (d) Dehazed result by Meng's method using L1-norm-based contextual regularization method [45]. (e) Dehazed result by Meng's method [45] using WGF. (f) Dehazed result using our proposed corrected transmission ($K = 50$).

when the pixel value in a hazy image is close to the global atmospheric light A, the pixel value of the recovered scene radiance J is much larger than C_0, which results in overestimating the recovered image. The transmission map in large bright areas needs to be corrected to tackle this problem. Thus, we introduce a tolerance factor K. If $|I - A| < K$, it is regarded as a white area, and the transmission map is corrected. Conversely, if $|I - A| > K$, the transmission map stays constant. As a result, the corrected transmission map is defined as

$$t_{true}(x) = \min\left(\max\left(\frac{K}{|I_B(x) - A|}, 1\right) \cdot \max\left(t(x), t_0\right), 1\right) \tag{16}$$

where t_0 is a small constant as the lower bound of the transmission map to preserve a small amount of haze in dense hazy region. As shown in Fig. 5(f), the overenhanced sky region is corrected, and the recovered haze-free image has a better visual effect than Fig. 5(e).

In addition, a correction based on the variance of estimated atmospheric light is implemented to prevent color distortion. When the variance of the estimated A is larger than a threshold, the color of the restored haze-free image is biased. Therefore, a corrected atmospheric light A_C is introduced for haze-free image recovery, which can be expressed as follows:

$$A_C = \begin{cases} \|A\| \cdot V_C, & \sigma_A^2 > \sigma_{\text{th}} \\ A, & else \end{cases} \tag{17}$$

where A and V_C are the initial estimated atmospheric light and the correction vector $(1/\sqrt{3}, 1/\sqrt{3}, 1/\sqrt{3})$, respectively. σ_A^2 and σ_{th} are the variance of A and the predefined threshold, respectively. A_C is the corrected atmospheric light. Then, the recovered haze-free base layer image $I'_B(x)$ can be expressed as follows:

$$I'_B(x) = \frac{I_B(x) - A}{\max(t_{\text{true}}(x), t_0)} + A_C \tag{18}$$

where $t_0 = 0.01$, which is the lower bound of transmission map.

Once the enhanced detailed layer I'_D and the dehazed base layer I'_B are obtained, the recovered haze-free image J is calculated as follows:

$$J(x) = I'_B(x) + I'_D(x). \tag{19}$$

As shown in Fig. 5(f), the recovered haze-free image obtained using the proposed method retains the fine detail, and the haze is removed.

IV. Experiments and Discussion

A. Experimental Settings

We use both synthetic RSHI datasets and real-world RSHI for evaluation. For synthetic datasets, we choose RICE-I [47] which includes 500 pairs of RSHIs with uniform haze. Also, a recently published large-scale realistic remote sensing dehazing

TABLE I
NOISE LEVEL ESTIMATION RESULTS ON THE REAL-WORLD REMOTE SENSING HAZY DATASET

True noise level	Rakhshanfar [49]			Liu [41]			Ours		
	Bias↓	Std↓	RMSE↓	Bias↓	Std↓	RMSE↓	Bias↓	Std↓	RMSE↓
1	0.032	0.034	0.092	0.069	0.044	0.082	**0.006**	**0.021**	**0.022**
5	**0.003**	0.296	0.296	0.029	0.021	**0.036**	0.068	**0.014**	0.042
10	0.072	0.187	0.200	**0.001**	0.035	0.035	0.021	**0.026**	**0.033**
20	0.033	0.270	0.272	0.050	0.064	0.081	**0.004**	**0.033**	**0.033**
30	0.090	0.445	0.454	0.127	0.107	0.166	**0.008**	**0.051**	**0.051**
40	0.226	0.584	0.626	0.220	0.114	0.248	**0.034**	**0.146**	**0.150**
50	0.353	0.779	0.856	0.318	0.148	0.350	**0.026**	**0.131**	**0.134**

The best value is in boldface.

dataset (RSHaze [48]) is selected for the nonuniform haze removal evaluation. The RSHaze contains RSHI with three haze densities: light, moderate, and dense. To verify the real-world image dehazing performance, we collected 30 real-world RSHI and aerial hazy image s from Google and Flickr as the real-world hazy dataset. As AGWN is one of the most dominant noises in a RSHI, we add the AGWN to the clean RSHI to get the noisy RSHI for the denoising test.

For noise level estimation evaluation, we choose Rakhshanfar's method [49], Liu's method [41], and Chen's method [7] for comparison. To evaluate the blind denoising performance, we integrate our noise level estimation method into two well-known nonblind denoising methods, BM3D [26] and FFDNet [26], for comparison. We select various state-of-the-art (SOTA) dehazing methods for dehazing comparison, including prior-based dehazing methods (DCP [14] and BCDP [50]), supervised-learning-based methods (AOD-Net [51], FFA-Net [52], and EMRA-Net [53]), and unsupervised-learning-based methods (YOLY [54] and ZID [55]). As there is no ground truth for real-world RSHI, we use the dehazing tool of Photoshop 2020 to generate the reference clear image for comparison. For a fair comparison, all the methods are implemented in MATLAB R2019a or PyCharm 2020 environment on a PC with an i7-9700F processor @3.00 GHz, 24 GB RAM, and a NVIDIA RTX 3080 GPU.

B. Noise Level Estimation Evaluation

To test the performance of the proposed noise level estimation method, we use our collected real-world RSHI dataset that includes 30 real-world remote sensing and aerial hazy images for evaluation. Synthetic AWGN with different noise levels (σ) is added to each hazy image, and the original hazy image is regarded as the noise-free image for measurement. As shown in Table I, we calculate bias, standard deviation (Std), and root mean square error (RMSE) for comparison. Std indicates the standard deviation of estimated noise levels. Bias and RMSE indicate the bias and RMSE between the estimated noise level and the true noise level, respectively. The bias and Std evaluate the accuracy and robustness of the noise level estimator respectively, while the RMSE reflects the overall performance.

Compared with Rakhshanfar's method [49] and Liu's method [41], our method is the most stable algorithm, with the lowest Std in estimating all ranks of the noise level. In terms of bias and RMSE, our method outperforms the other two methods in most ranks of the noise level. This indicates that the proposed noise level estimation method is more accurate and stable than the other methods.

TABLE II
EXECUTION TIME (UNIT: S) OF DIFFERENT NOISE LEVEL ESTIMATION METHODS

Resolution	Rakhshanfar [49]	Liu [41]	Chen [7]	Ours
1024 × 768	0.011	6.206	0.074	**0.005**
4096 × 3072	0.045	22.837	0.279	**0.017**

The best value is in boldface and our proposed method is the fastest.

TABLE III
PROCESSING TIME COMPARISON OF BM3D AND FFDNET INTEGRATED WITH OUR NOISE LEVEL ESTIMATION METHOD (UNIT: S)

Resolution	BM3D (CPU)	FFDNet (CPU)	FFDNet (GPU)
600 × 400	7.515	0.245	0.001
800 × 600	23.287	0.491	0.001
1024 × 768	29.674	0.887	0.001
1600 × 1200	86.352	2.081	0.002
2048 × 1536	161.969	3.518	0.003
3200 × 2400	403.691	8.622	0.005
4096 × 3072	631.445	15.028	0.006

To evaluate the computation complexity, we compare the execution time of the proposed method with different methods [7], [41], [49]. A total of 30 noisy images in different scenes with a resolution of 1024 × 768 and 4096 × 3072 are selected, and the average processing time is calculated. As shown in Table II, our proposed method has the smallest processing time, which is almost 1300 times faster than Liu's method [41]. Even compared with Chen's method [7], which has a similar noise level estimation principle, our method improves the efficiency by 15 times. Therefore, our proposed method has high efficiency and can estimate the noise level for a 4K resolution video at a speed of over 50 frames per second.

C. Blind Denoising Evaluation

In this section, we integrate the proposed noise level estimation method into two nonblind denoising methods [17], [26] to achieve blind denoising. As shown in Fig. 7, we choose a noise-free image from our collected real-world remote sensing hazy dataset. Then, Gaussian noise with a noise level (σ) from 1 to 100 at a step of 2 is added to the image. The noisy images are denoised by BM3D [26] and FFDNet [17] with the true noise level and with our estimated noise level, respectively.

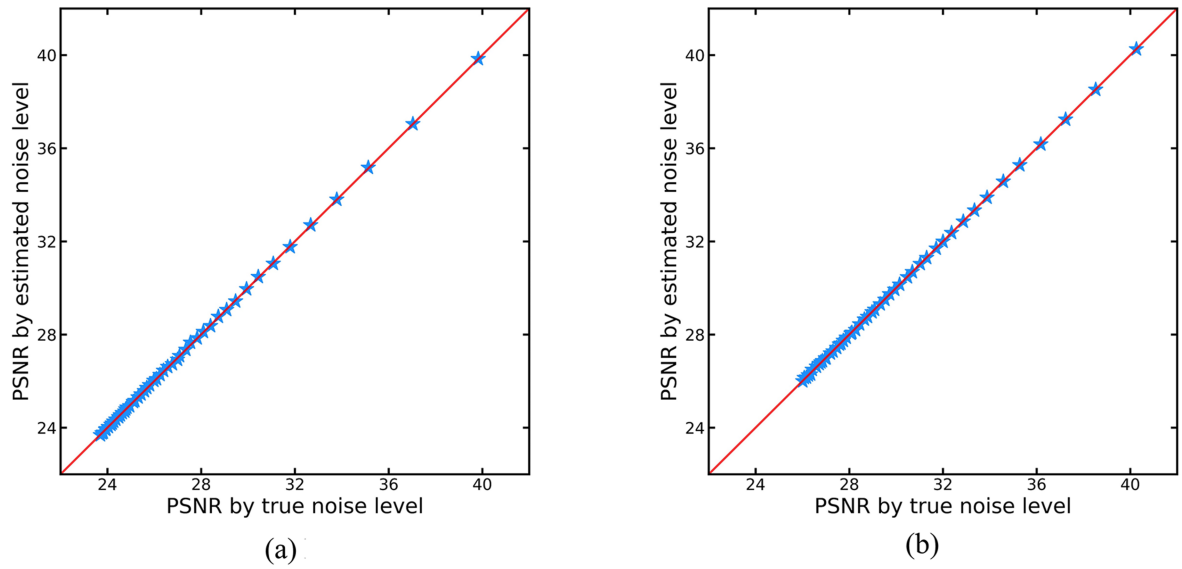

Fig. 6. Comparison of the denoising performance of BM3D and FFDNet with the true noise level and our estimated noise level.

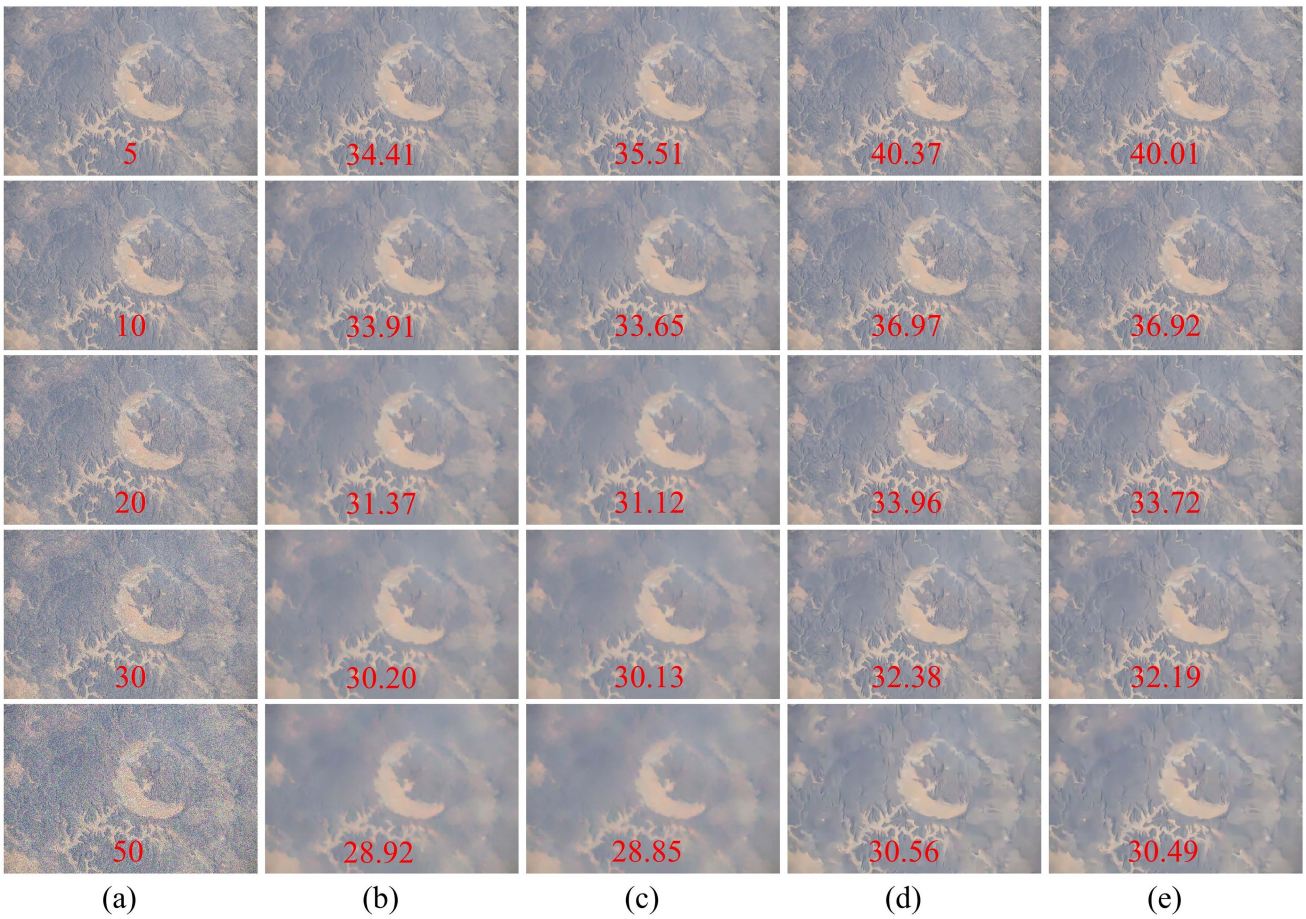

Fig. 7. Comparison of the denoising results by BM3D [26] and FFDNet [17] with the true noise level and our estimated noise level, where (a) is the noisy image with different noise level from 5 to 50, (b) to (e) are the denoised results using (b) BM3D with the true noise level, (c) BM3D with our estimated noise level, (d) FFDNet with the true noise level, and (e) FFDNet with our estimated noise level. The noise level and PSNR value are marked by red in (a) and (b) to (e), respectively.

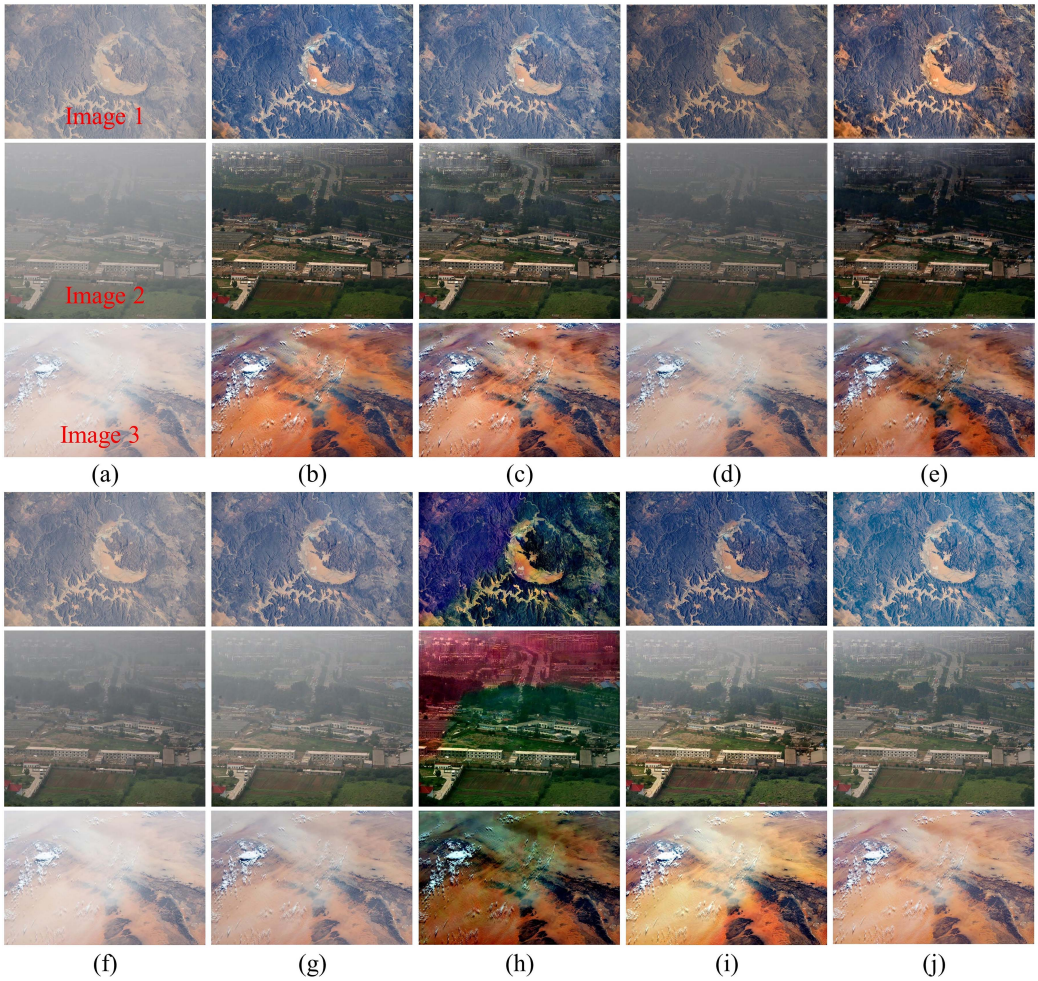

Fig. 8. Comparison of various dehazing methods on real-world RSHIs and aerial hazy images, where (a) is the hazy input, (b) to (j) are the dehazed results by (b) DCP [14], (c) BCDP [50], (d) AOD-Net [51], (e) EMRA-Net [53], (f) FFANet [52], (g) YOLY [54], (h) ZID [55], (i) ours, and (j) Photoshop.

As shown in Fig. 6, we compare the PSNR between the noisy image and the denoised image. The performance of both BM3D and FFDNet with our estimated noise level is almost the same as that of the true noise level. One can also see that FFDNet had better performance, with a higher average PSNR. Therefore, the proposed method can be integrated into the nonblind denoising method without reducing the denoising performance.

Samples of the denoised images are shown in Fig. 7, where Fig. 7(a) shows the noisy images, with different noise levels (σ) marked in red. Fig. 7(b)–(e) shows the denoised images by BM3D and FFDNet with the true noise level and with our estimated noise level, and the PSNR value is marked in red. As shown in Fig. 7, the visual effect and PSNR value of the denoised image by BM3D and FFDNet with true or estimated noise level are almost the same, which indicates that our proposed method is effective for accurate noise level estimation. Also, one can find that the FFDNet outperformed the BM3D, with a higher PSNR and better visual effects. When the noise level is over 20, BM3D can hardly recover the fine details, while the FFDNet can better recover the clean hazy image. Therefore, we integrate the proposed noise level estimation method into the FFDNet to achieve blind denoising before the following dehazing.

In addition, we compared the time complexity of BM3D and FFDNet when combined with our noise level estimation method. Table III compares the processing time of BM3D and FFDNet for noisy hazy images with resolutions ranging from 600×400 to 4096×3072. The BM3D is executed solely on the CPU, whereas the FFDNet is evaluated in CPU mode and GPU mode. Using only CPU, the results demonstrate that denoising time grows as image size increases. However, the computation efficiency of FFDNet is vastly superior than that of BM3D, requiring much less processing time. In addition, GPU can significantly accelerate the processing of FFDNet, and the processing time is less dependent on the image size when utilizing GPU.

D. Dehazing Evaluation

To test performance, both qualitative and quantitative evaluations are conducted. We compare our method with well-known dehazing methods to evaluate the reliability and design progress,

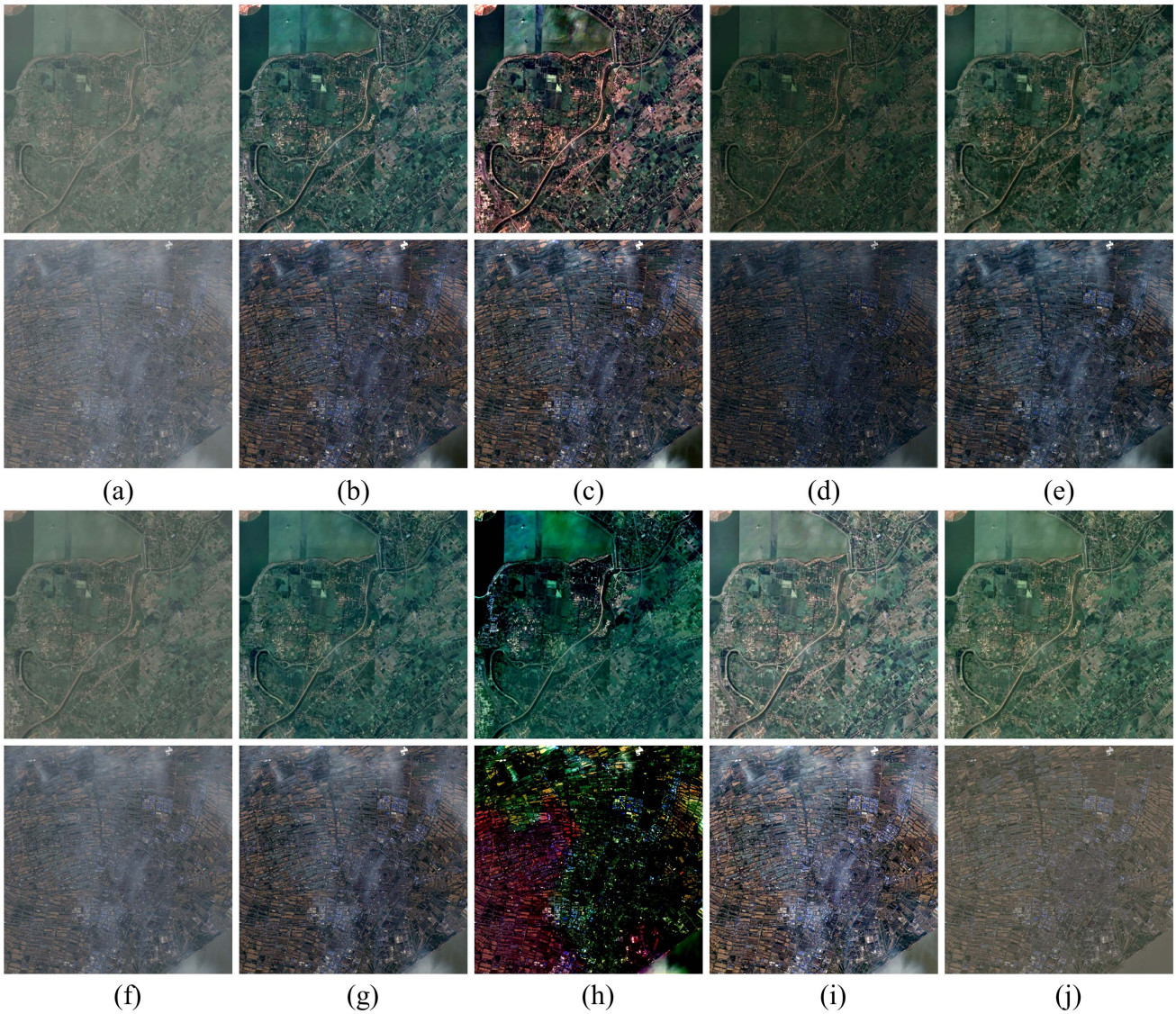

Fig. 9. Comparison of synthetic RSHI datasets, where the first and second rows are the images selected from RICE-I [47] and RSHaze [48], respectively. (a) is the hazy input, (b) to (j) are the dehazed results by (b) DCP [14], (c) BCDP [50], (d) AOD-Net [51], (e) EMRA-Net [53], (f) FFANet [52], (g) YOLY [54], (h) ZID [55], (i) ours, and (j) ground truth.

including prior-based dehazing methods (DCP [14] and BCDP [50]), supervised-learning-based methods (AOD-Net [51], FFA-Net [52], and EMRA-Net [53]), and unsupervised-learning-based methods (YOLY [54] and ZID [55]). We use real-world RSHI for qualitative comparison and synthetic RSHI datasets for quantitative evaluation.

From Fig. 8(h), the ZID obtains the worst dehazing result with severe color distortion. The dehazed images by EMRA-Net have dark color [see the "Image 2" of Fig. 8(e)]. As shown in Fig. 8(d), (f), and (g), the AOD-Net, FFANet, and YOLY have poor dehazing performance with a lot of residual haze in the dehazed image. The DCP, BCDP, and our method achieve visually better dehazing effects among the various dehazing methods. However, the DCP may result in dark color as shown in Fig. 8(b), while the BCDP has slight overenhancement [see "Image 2" in Fig. 8(c)]. Compared with the other dehazing methods, the dehazed results by our method look closer to the reference images by Photoshop in Fig. 8(j).

We selected RICE-I [47] and RSHaze [48] to conduct the quantitative evaluation. For uniform dehazing evaluation, we test the whole RICE-I. For the nonuniform dehazing test, we randomly select 50 hazy images for each haze density from RSHaze, so we have 150 images in total. We choose the PSNR, SSIM, and LPIPS to quantitively measure the dehazing performance. The definition of PSNR is given as follows:

$$\text{PSNR} = 20 \lg \frac{L-1}{\sqrt{\text{MSE}}} \tag{20}$$

where L is the dynamic range of image and MSE is the mean square error. The expression of SSIM is as follows:

$$\text{SSIM}(I_1, I_2) = L(I_1, I_2) * C(I_1, I_2) * S(I_1, I_2) \tag{21}$$

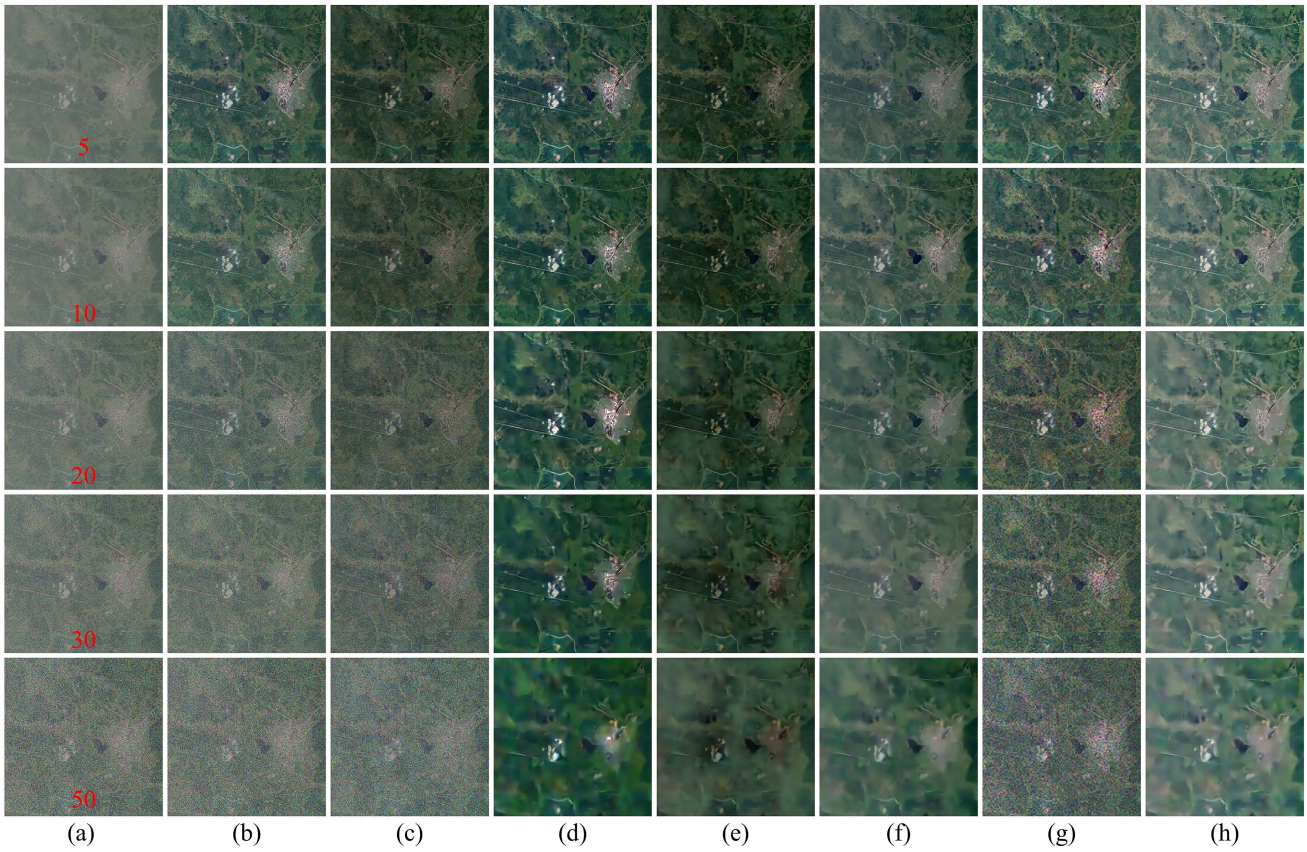

Fig. 10. Comparison of joint denoising and dehazing using different methods. The first row to fifth row of (a) is the noisy hazy images with different noise levels marked in red, and (a)–(h) are the recovered results by different methods. (a) Input noisy hazy images. (b) DCP [14]. (c) EMRA-Net [53]. (d) FFDNet+DCP. (e) FFDNet+EMRA-Net. (f) FFDNet+YOLY [54]. (g) HSU et al [36]. (h) Ours.

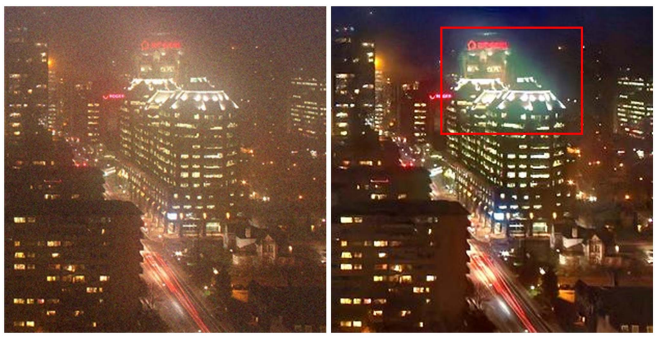

Fig. 11. Failure case of the proposed method in processing nighttime noisy hazy image.

where L, C, and S are the luminance comparison, contrast comparison, and structure comparison, respectively. Higher PSNR and SSIM values indicate better image quality. Using a predefined deep neural network [56], the LPIPS is estimated to determine the perceptual similarity between two images. A lower LPIPS refers to the closer perceptual similarity between the restored image and the ground truth. As shown in Table IV, our method obtains the best results for the three metrics on average, which indicates that our method outperforms the other methods in removing both uniform haze and nonuniform haze. In addition, we can find that DCP, EMRA-Net, and YOLY obtain the best result in the prior-based category, supervised-learning-based category, and unsupervised-based category, respectively. Samples of the dehazed results on synthetic remote sensing hazy datasets are shown in Fig. 9. One can find that the BCDP and ZID suffer from color distortion. The AOD-Net and EMRA-Net result in dark color, while the FFANet cannot remove haze properly. The DCP, YOLY, and our method obtain visually better dehazed results.

E. Joint Denoising and Dehazing Evaluation

In this section, we conduct the joint denoising and dehazing evaluation. As discussed in Sections IV-C and IV-D, we find that the FFDNet [17] have better denoising performance, while DCP [14], EMRA-Net [53], and YOLY [54] obtain the best result in the prior-based category, supervised-learning-based category, and unsupervised-based category, respectively. Therefore, we compare our proposed method with pure dehazing methods (DCP, EMRA-Net, and YOLY) and combined the FFDNet with these dehazing methods for evaluation. Note that we integrate our noise level estimation method into FFDNet as the blind denoising module (see Fig. 1 in Section III), and the other methods use the true noise level with FFDNet for denoising.

TABLE IV
QUANTITATIVE EVALUATION ON SYNTHETIC REMOTE SENSING HAZY DATASETS (RICE-I [47] AND RSHAZE [48])

Method	RICE-I			RSHaze			Average		
	PSNR ↑	SSIM ↑	LPIPS ↓	PSNR ↑	SSIM ↑	LPIPS ↓	PSNR ↑	SSIM ↑	LPIPS ↓
DCP	18.73	0.796	0.197	**18.35**	0.746	0.249	18.54	0.771	0.223
BCDP	16.12	0.665	0.298	17.49	0.699	0.283	16.81	0.682	0.290
AOD-Net	14.84	0.679	0.150	15.68	0.689	0.256	15.26	0.684	0.203
EMRA-Net	19.90	0.824	0.118	15.96	0.627	0.239	17.93	0.725	0.179
FFANet	16.59	0.771	0.083	15.26	0.752	0.278	15.92	0.762	0.180
YOLY	19.83	0.853	**0.080**	16.01	0.713	0.258	17.92	0.783	0.169
ZID	13.42	0.530	0.339	14.80	0.539	0.312	14.11	0.535	0.325
Ours	**20.68**	**0.877**	0.092	18.21	**0.810**	**0.205**	**19.45**	**0.843**	**0.148**

The best value and the second-best value of the specific index are in boldface and underlined, respectively.

TABLE V
QUANTITATIVE EVALUATION RESULTS OF JOINT DENOISING AND DEHAZING ON RICE-I DATASETS

Method	PSNR with different noise levels					SSIM with different noise levels				
	5	10	20	30	50	5	10	20	30	50
DCP	19.93	19.70	18.92	18.09	17.07	0.548	0.451	0.367	0.308	0.260
EMRANet	18.79	19.10	18.89	18.23	17.15	0.662	0.559	0.450	0.372	0.309
YOLY	18.55	17.70	16.66	16.01	15.30	0.536	0.429	0.336	0.275	0.230
FFDNet+DCP	18.96	18.69	18.37	18.07	17.76	0.804	**0.781**	0.748	0.718	0.685
FFDNet+EMRANet	16.72	16.47	16.61	16.79	17.01	0.737	0.707	0.683	0.662	0.643
FFDNet+YOLY	19.55	19.52	19.45	19.39	19.30	0.774	0.756	0.731	0.709	0.685
HSU's method	19.11	18.94	18.56	18.13	17.21	0.782	0.675	0.513	0.314	0.267
Ours	**20.26**	**19.98**	**19.90**	**19.84**	**19.75**	**0.820**	0.777	**0.752**	**0.730**	**0.704**

The best value and the second-best value of the specific index are in boldface and underlined, respectively.

In addition, an SOTA joint dehazing and denoising algorithms proposed by Hsu et al. [36] is chosen for comparison. Hsu et al. [36] extracted the image's low-frequency component for dehazing by WT, while the other high-frequency components are denoised. To achieve quantitative evaluation, we randomly selected 50 RSHIs from RICE-I and added AWGN with five noise levels ($\sigma \in \{5, 10, 20, 30, 50\}$), giving us a total of 250 noisy RSHIs for testing.

As shown in Table V, we found that the joint denoising and dehazing had a higher PSNR and SSIM than pure dehazing in most cases. Moreover, the change in SSIM is more sensitive than that of PSNR when the noise increased. Thus, when there is much noise in RSHI, joint denoising and dehazing will significantly improve the recovered image's quality. Also, HSU's method [36] cannot well remove the noise in high-frequency domain, which indicates poor results for high noise level. Our proposed method achieves the best results for both PSNR and SSIM index in all ranks of noise level, except the second-best SSIM value in the noise level of 10. Therefore, our method is superior to the other methods in joint denoising and dehazing evaluation.

Fig. 10(a) shows the noisy hazy images with different noise levels (σ) marked in red, and (b)–(h) are the recovered results by various methods. The results by DCP, EMRA-Net, and YOLY have severe noise. By combining the FFDNet as preprocessing, the noise is removed, and the visual effect is significantly improved. However, both FFDNet+DCP and FFDNet+EMRANet produce a loss of detailed information in darker areas or under extremely noisy circumstances, while the FFDNet+YOLY cannot remove haze thoroughly. As denoising is only operated on high-frequency parts, HSU's method obtains poor results when the noise level is over 10. Overall, the proposed method has better performance in both denoising and dehazing.

F. Discussions

Based the results of extensive experiments, our proposed noise level estimation approach is effective and efficient to be integrated into nonblind image denoising algorithms. The multiscale decomposition enables the operation of dehazing and detail enhancement independently, which is sufficient for the preservation of image details. In addition, the joint denoising and dehazing evaluation reveals that denoising prior to dehazing can greatly improve the image's quality. Nevertheless, our proposed algorithm cannot effectively recover nighttime images that are noisy and hazy. As shown in Fig. 11, even although the noise has been greatly reduced, the low-light imaging conditions have resulted in the loss of image's details. Moreover, the glow caused by artificial light may contribute unwanted artifacts into the recovered result. Consequently, our proposed algorithm for joint denoising and dehazing needs be enhanced for nighttime or low-light image recovery, which is the subject of our future article.

V. CONCLUSION

In response to the problem of details lost and noise amplification in RSID, we propose a novel image recovery and enhancement method by joint denoising and dehazing.

As preprocessing, a simple but effective noise level estimation method based on a quad-tree subdivision algorithm is implemented, and FFDNet denoising is performed to improve the hazy image. The denoised hazy image is decomposed into base and detailed layers to preserve the sharp details using a multiscale GF. The dehazing method based on the corrected boundary constraint is implemented in the base layer, and the detailed layers are enhanced by a sigmoid-based nonlinear mapping function. Therefore, the haze can be removed without losing the sharp details. Finally, the enhanced detailed layers and the dehazed base layer are fused to obtain the recovered image. Overall, the results show that the proposed dehazing method offers three benefits: 1) good blind denoising performance with accurate and efficient noise level estimation; 2) remarkable quantitative results for PSNR, SSIM, and LPIPS indices on RSHI datasets; and 3) superior performance for joint denoising and dehazing evaluation.

REFERENCES

[1] W. Zhao, Y. Lv, Q. Liu, and B. Qin, "Detail-preserving image denoising via adaptive clustering and progressive PCA thresholding," *IEEE Access*, vol. 6, pp. 6303–6315, 2018.

[2] Q. Yi, A. Jiang, J. Li, J. Wan, and M. Wang, "Progressive back-traced dehazing network based on multi-resolution recurrent reconstruction," *IEEE Access*, vol. 8, pp. 54514–54521, 2020.

[3] J. Wei, Y. Wu, L. Chen, K. Yang, and R. Lian, "Zero-shot remote sensing image dehazing based on a re-degradation haze imaging model," *Remote Sens.*, vol. 14, no. 22, 2022, Art. no. 5737.

[4] G. Sahu, A. Seal, D. Bhattacharjee, M. Nasipuri, P. Brida, and O. Krejcar, "Trends and prospects of techniques for haze removal from degraded images: A survey," *IEEE Trans. Emerg. Topics Comput. Intell.*, vol. 6, no. 4, pp. 762–782, Aug. 2022.

[5] Y. Liu, P. Jia, H. Zhou, and A. Wang, "Joint dehazing and denoising for single nighttime image via multi-scale decomposition," *Multimedia Tools Appl.*, vol. 81, pp. 23941–23962, 2022.

[6] P. Jiang, Q. Wang, and J. Wu, "Efficient noise-level estimation based on principal image texture," *IEEE Trans. Circuits Syst. Video Technol.*, vol. 30, no. 7, pp. 1987–1999, Jul. 2020.

[7] G. Chen, F. Zhu, and P. Ann Heng, "An efficient statistical method for image noise level estimation," in *Proc. IEEE Conf. Comput. Vis.*, 2015, pp. 477–485.

[8] E. J. McCartney, "Optics of the atmosphere: Scattering by molecules and particles," *Phys. Bull.*, vol. 28, no. 11, pp. 1–421, 1976.

[9] F. A. Dharejo, Y. Zhou, F. Deeba, M. A. Jatoi, Y. Du, and X. Wang, "A remote-sensing image enhancement algorithm based on patch-wise dark channel prior and histogram equalisation with colour correction," *IET Image Process.*, vol. 15, no. 1, pp. 47–56, 2021.

[10] X. Zheng, T. Gong, X. Li, and X. Lu, "Generalized scene classification from small-scale datasets with multitask learning," *IEEE Trans. Geosci. Remote Sens.*, vol. 60, 2022, Art. no. 5609311.

[11] X. Zheng, H. Sun, X. Lu, and W. Xie, "Rotation-invariant attention network for hyperspectral image classification," *IEEE Trans. Image Process.*, vol. 31, pp. 4251–4265, 2022.

[12] Y. Zheng, J. Su, S. Zhang, M. Tao, and L. Wang, "Dehaze-AGGAN: Unpaired remote sensing image dehazing using enhanced attention-guide generative adversarial networks," *IEEE Trans. Geosci. Remote Sens.*, vol. 60, 2022, Art. no. 5630413.

[13] X. Chen and Y. Huang, "Memory-oriented unpaired learning for single remote sensing image dehazing," *IEEE Trans. Geosci. Remote Sens.*, vol. 19, 2022, Art. no. 3511705.

[14] K. He, J. Sun, and X. Tang, "Single image haze removal using dark channel prior," *IEEE Trans. Pattern Anal. Mach. Intell.*, vol. 33, no. 12, pp. 2341–2353, Dec. 2011.

[15] H. Zhang and V. M. Patel, "Densely connected pyramid dehazing network," in *Proc. IEEE Conf. Comput. Vis. Pattern Recognit.*, 2018, pp. 3194–3203.

[16] Q. Wu, W. Ren, and X. Cao, "Learning interleaved cascade of shrinkage fields for joint image dehazing and denoising," *IEEE Trans. Image Process.*, vol. 29, pp. 1788–1801, 2020.

[17] K. Zhang, W. Zuo, and L. Zhang, "FFDNet: Toward a fast and flexible solution for CNN-based image denoising," *IEEE Trans. Image Process.*, vol. 27, no. 9, pp. 4608–4622, Sep. 2018.

[18] M. Ju, C. Ding, D. Zhang, and Y. J. Guo, "Gamma-correction-based visibility restoration for single hazy images," *IEEE Signal Process. Lett.*, vol. 25, no. 7, pp. 1084–1088, Jul. 2018.

[19] W. Ni, X. Gao, and Y. Wang, "Single satellite image dehazing via linear intensity transformation and local property analysis," *Neurocomputing*, vol. 175, pp. 25–39, 2016.

[20] D. Berman and S. Avidan, "Non-local image dehazing," in *Proc. IEEE Conf. Comput. Vis. Pattern Recognit.*, 2016, pp. 1674–1682.

[21] Q. Zhu, J. Mai, and L. Shao, "A fast single image haze removal algorithm using color attenuation prior," *IEEE Trans. Image Process.*, vol. 24, no. 11, pp. 3522–3533, Nov. 2015.

[22] B. Jiang et al., "Deep dehazing network for remote sensing image with non-uniform haze," *Remote Sens.*, vol. 13, no. 21, 2021, Art. no. 4443.

[23] P. Dong and B. Wang, "TransRA: Transformer and residual attention fusion for single remote sensing image dehazing," *Multidimensional Syst. Signal Process.*, vol. 33, pp. 1–20, 2022.

[24] X. Chen, Y. Li, L. Dai, and C. Kong, "Hybrid high-resolution learning for single remote sensing satellite image dehazing," *IEEE Geosci. Remote Sens. Lett.*, vol. 19, 2021, Art. no. 6002805.

[25] R. Chen, D. Pu, Y. Tong, and M. Wu, "Image-denoising algorithm based on improved K-singular value decomposition and atom optimization," *CAAI Trans. Intell. Technol.*, vol. 7, no. 1, pp. 117–127, 2022.

[26] K. Dabov, A. Foi, V. Katkovnik, and K. Egiazarian, "Image denoising by sparse 3-D transform-domain collaborative filtering," *IEEE Trans. Image Process.*, vol. 16, no. 8, pp. 2080–2095, Aug. 2007.

[27] A. Mustafi and S. Ghorai, "A novel blind source separation technique using fractional Fourier transform for denoising medical images," *Optik*, vol. 124, no. 3, pp. 265–271, 2013.

[28] S. Sardy, P. Tseng, and A. Bruce, "Robust wavelet denoising," *IEEE Trans. Signal Process.*, vol. 49, no. 6, pp. 1146–1152, Jun. 2001.

[29] Q. Zhang, J. Xiao, C. Tian, J. C.-W. Lin, and S. Zhang, "A robust deformed convolutional neural network (CNN) for image denoising," *CAAI Trans. Intell. Technol.*, to be published, doi: 10.1049/cit2.12110.

[30] K. Zhang, W. Zuo, Y. Chen, D. Meng, and L. Zhang, "Beyond a Gaussian denoiser: Residual learning of deep CNN for image denoising," *IEEE Trans. Image Process.*, vol. 26, no. 7, pp. 3142–3155, Jul. 2017.

[31] X. Feng, W. Zhang, X. Su, and Z. Xu, "Optical remote sensing image denoising and super-resolution reconstructing using optimized generative network in wavelet transform domain," *Remote Sens.*, vol. 13, no. 9, 2021, Art. no. 1858.

[32] C. Ren, X. He, C. Wang, and Z. Zhao, "Adaptive consistency prior based deep network for image denoising," in *Proc. IEEE Conf. Comput. Vis. Pattern Recognit.*, 2021, pp. 8596–8606.

[33] A. Yang, H. Wang, Z. Ji, Y. Pang, and L. Shao, "Dual-path in dual-path network for single image dehazing," in *Proc. Int. Joint Conf. Artif. Intell.*, 2019, pp. 4627–4634.

[34] X. Liu, H. Zhang, Y.-M. Cheung, X. You, and Y. Y. Tang, "Efficient single image dehazing and denoising: An efficient multi-scale correlated wavelet approach," *Comput. Vis. Image Understanding*, vol. 162, pp. 23–33, 2017.

[35] E. Matlin and P. Milanfar, "Removal of haze and noise from a single image," in *Proc. Comput. Imag. X*, 2012, pp. 177–188.

[36] W.-Y. Hsu and Y.-S. Chen, "Single image dehazing using wavelet-based haze-lines and denoising," *IEEE Access*, vol. 9, pp. 104547–104559, 2021.

[37] W. Su, Y. Zhang, H. Wei, and Q. Gao, "Denoising and dehazing an image in a cascaded pattern for continuous casting," *Metals*, vol. 12, no. 1, 2022, Art. no. 126.

[38] B. Xu and H. Yin, "A slimmer and deeper approach to network structures for image denoising and dehazing," in *Proc. Int. Conf. Intell. Data Eng. Automat. Learn.*, 2020, pp. 268–279.

[39] K. Zhang, W. Zuo, S. Gu, and L. Zhang, "Learning deep CNN denoiser prior for image restoration," in *Proc. IEEE Conf. Comput. Vis. Pattern Recognit.*, 2017, pp. 3929–3938.

[40] S. Pyatykh, J. Hesser, and L. Zheng, "Image noise level estimation by principal component analysis," *IEEE Trans. Image Process.*, vol. 22, no. 2, pp. 687–699, Feb. 2013.

[41] X. Liu, M. Tanaka, and M. Okutomi, "Single-image noise level estimation for blind denoising," *IEEE Trans. Image Process.*, vol. 22, no. 12, pp. 5226–5237, Dec. 2013.

[42] K. He, J. Sun, and X. Tang, "Guided image filtering," *IEEE Trans. Pattern Anal. Mach. Intell.*, vol. 35, no. 6, pp. 1397–1409, Jun. 2013.

[43] Y. Cho, J. Jeong, and A. Kim, "Model-assisted multiband fusion for single image enhancement and applications to robot vision," *IEEE Robot. Automat. Lett.*, vol. 3, no. 4, pp. 2822–2829, Oct. 2018.
[44] R. T. Tan, "Visibility in bad weather from a single image," in *Proc. IEEE Conf. Comput. Vis. Pattern Recognit.*, 2008, pp. 1–8.
[45] G. Meng, Y. Wang, J. Duan, S. Xiang, and C. Pan, "Efficient image dehazing with boundary constraint and contextual regularization," in *Proc. IEEE Conf. Comput . Vis.*, 2013, pp. 617–624.
[46] Z. Li, J. Zheng, Z. Zhu, W. Yao, and S. Wu, "Weighted guided image filtering," *IEEE Trans. Image Process.*, vol. 24, no. 1, pp. 120–129, Jan. 2015.
[47] D. Lin, G. Xu, X. Wang, Y. Wang, X. Sun, and K. Fu, "A remote sensing image dataset for cloud removal," 2019, *arXiv:1901.00600*.
[48] Y. Song, Z. He, H. Qian, and X. Du, "Vision transformers for single image dehazing," 2022, *arXiv:2204.03883*.
[49] M. Rakhshanfar and M. A. Amer, "Estimation of Gaussian, Poissonian–Gaussian, and processed visual noise and its level function," *IEEE Trans. Image Process.*, vol. 25, no. 9, pp. 4172–4185, Sep. 2016.
[50] X. Zhao, "Single image dehazing using bounded channel difference prior," in *Proc. IEEE Conf. Comput. Vis. Pattern Recognit.*, 2021, pp. 727–735.
[51] B. Li, X. Peng, Z. Wang, J. Xu, and D. Feng, "Aod-net: All-in-one dehazing network," in *Proc. IEEE Conf. Comput. Vis.*, 2017, pp. 4770–4778.
[52] X. Qin, Z. Wang, Y. Bai, X. Xie, and H. Jia, "FFA-Net: Feature fusion attention network for single image dehazing," in *Proc. AAAI Conf. Artif. Intell.*, vol. 34, no. 7, pp. 11908–11915, 2020.
[53] J. Wang, C. Li, and S. Xu, "An ensemble multi-scale residual attention network (EMRA-net) for image dehazing," *Multimedia Tools Appl.*, vol. 80, no. 19, pp. 29299–29319, 2021.
[54] B. Li, Y. Gou, S. Gu, J. Z. Liu, J. T. Zhou, and X. Peng, "You only look yourself: Unsupervised and untrained single image dehazing neural network," *Int. J. Comput. Vis.*, vol. 129, no. 5, pp. 1754–1767, 2021.
[55] B. Li, Y. Gou, J. Z. Liu, H. Zhu, J. T. Zhou, and X. Peng, "Zero-shot image dehazing," *IEEE Trans. Image Process.*, vol. 29, pp. 8457–8466, 2020.
[56] R. Zhang, P. Isola, A. A. Efros, E. Shechtman, and O. Wang, "The unreasonable effectiveness of deep features as a perceptual metric," in *Proc. IEEE Conf. Comput. Vis. Pattern Recognit.*, 2018, pp. 586–595.

Yan Cao received the M.S. degree in statistics in 2016 from Fujian Agriculture and Forestry University, Fuzhou, China, where she is currently working toward the Ph.D. degree in forest management with the College of Forestry.

She is currently a Lecturer with the College of Finance, Fujian Jiangxia University, Fuzhou, China. Her research interests include machine learning, computer vision, and related problems.

Jianchong Wei received the B.E. degree in electronic information engineering from Fuzhou University, Fuzhou, China, in 2014, and the M.S. degree in signal and information processing from Fuzhou University, Fuzhou, China, in 2017.

He is currently a Lecturer with the College of Electronics and Information Science, Fujian Jiangxia University, Fuzhou, China. His research interests include image dehazing, image denoising, and related vision problems.

Sifan Chen received the bachelor's degree in electronic information engineering in 2020 from Fuzhou University, Fuzhou, China, where he is currently working toward the master's degree in electronics and communication engineering.

His research interests include multisensor fusion and autonomous flight of unmanned aerial vehicle.

Baihe Chen received the master's degree in integrated circuit engineering from Fuzhou University, Fuzhou, China, in 2022.

She is currently a Teacher with the School of Modern Information Industry, Guangzhou College of Commerce, Guangzhou, China. Her research interests include artificial intelligence, fully autonomous UAV, path planning of UAV, etc.

Zhensheng Wang received the Ph.D. degree in geographical information science from Wuhan University, Wuhan, China, in 2015.

He is currently an Associate Researcher with Peng Cheng Laboratory, Shenzhen, China. His research interests include geospatial artificial intelligence and spatial analysis.

Zhaohui Liu received the Ph.D. degree in urban planning from Tongji University, Shanghai, China, in 2015.

He is currently a part-time Researcher with Peng Cheng Laboratory, Shenzhen, China, and a Professor and an Assistant Secretary-General with China Society for Urban Studies. His research interests include smart cities and urban dynamics analysis.

Chengbin Chen received the Ph.D. degree in communication and information system from Fuzhou University, Fuzhou, China, in 2022.

He is currently a Postdoctor with Peng Cheng Laboratory, Shenzhen, China. His research interests include multiagent collaborative, UAV control system, trajectory prediction, and path planning.